Tunable broad light emission from 3D "Hollow" Bromide Perovskites through Defect Engineering

Ioannis Spanopoulos, Ido Hadar, Weijun Ke, Peijun Guo, Eve Mozur, Emily Morgan, Shuxin Wang, Ding Zheng, Suyog Padgaonkar, G. Manjunatha Reddy, et al.

Tunable broad light emission from 3D "Hollow" Bromide Perovskites through Defect Engineering

Ioannis Spanopoulos[1], Ido Hadar[1&], Weijun Ke[1§], Peijun Guo[2#], Eve M. Mozur,[3] Emily Morgan,[3] Shuxin Wang,[3] Ding Zheng,[1] Suyog Padgaonkar,[4] G. N. Manjunatha Reddy,[5] Emily A. Weiss,[4] Mark C. Hersam,[6] Ram Seshadri,[3] Richard D. Schaller[1], and Mercouri G. Kanatzidis*,[1]

[1]*Department of Chemistry, Northwestern University, Evanston, Illinois 60208, United States*
[2]*Center for Nanoscale Materials, Argonne National Laboratory, 9700 South Cass Avenue, Lemont, Illinois 60439, United States*
[3]*Materials Department and Materials Research Laboratory, University of California, Santa Barbara, California 93106, United States*
[4]*Department of Chemistry and the Materials Research Center, Applied Physics Program, and Department of Materials Science and Engineering and the Materials Research Center, Northwestern University, Evanston, Illinois 60208, United States*
[5]*University of Lille, CNRS, Centrale Lille Institut, Univ. Artois, UMR8181-UCCS-Unité de Catalyse et Chimie du Solide, F-59000 Lille, France.*
[6]*Department of Materials Science and Engineering, Department of Chemistry, Department of Electrical and Computer Engineering, and the Materials Research Center, Northwestern University, Evanston, Illinois 60208, United States*

ABSTRACT

Hybrid halide perovskites consisting of corner-sharing metal halide octahedra and small cuboctahedral cages filled with counter cations have proven to be prominent candidates for many high-performance optoelectronic devices. The stability limits of their three-dimensional perovskite structure are defined by the size range of the cations present in the cages of the structure. In some cases, the stability of the perovskite structure can be extended even when the counter ions violate the size and shape requirements, as for example in the so-called "hollow" perovskites. In this work we take advantage of this property to engineer a new family of 3D highly defective yet crystalline "hollow" bromide perovskites with general formula $(FA)_{1-x}(en)_x(Pb)_{1-0.7x}(Br)_{3-0.4x}$ (FA = formamidinium, *en* = ethylenediammonium, x = 0-0.44). The materials were characterized by a battery of techniques, including single crystal X-ray diffraction (XRD), high resolution powder X-ray diffraction (PXRD), and solid state nuclear magnetic resonance (NMR) measurements. Pair distribution function (PDF) analysis shed light on the local structural coherence, revealing a wide distribution of Pb-Pb distances in the crystal structure a consequence of the Pb/Br-deficient nature and *en* inclusion in the lattice. By manipulating the number of Pb/Br vacancies, we finely tune the optical properties of the pristine 3D $FAPbBr_3$, by blue shifting the band gap from 2.20 eV up to 2.60 eV for the 0.42 *en* sample. A most unexpected outcome was

that at x> 0.40 *en* incorporation the material exhibits strong broad light emission with 1% photoluminescence quantum yield (PLQY), that is maintained after exposure in air for more than a year. This is the first example of strong broad light emission from a 3D hybrid halide perovskite. We conclude that "hollowness" as expressed by Pb and Br vacancies, is a robust state of 3D perovskites and can offer new optoelectronic features.

INTRODUCTION

Halide perovskites have the potential to be the next generation semiconductors[1-3] with exquisite fine tunable optoelectronic properties[4-5] directly deriving from their unique structural configuration and chemical versatility.[6-7] The most investigated until today are the 3D perovskite materials with the general formula AMX_3 ($A = CH_3NH_3^+$ (MA), $HC(NH_2)_2^+$ (FA), Cs^+; $M = Ge^{2+}$, Sn^{2+}, Pb^{2+}; $X = Cl^-$, Br^-, I^-).[8,9] The aristotype perovskite structure consists of MX_6 corner sharing metal halide octahedra that span to three orthogonal directions, while A^+ cations reside in the formed cuboctahedral cavities charge balancing the structure.[10] Among the attractive features of this perovskites family are solution processability, long carrier lifetimes[11] and diffusion lengths,[12-13] as well promising high tolerance for radiation damage.[14-16] Nonetheless, these traits derive from the defect tolerant character of these materials.[17-20] Apparently, the majority of point defects are shallow, close to the band edges and do not act as significant traps for the generated carriers.[21-22]

Defect engineering in perovskites could add extra handles in tailoring their structures, optoelectronic properties and long-term environmental stability.[23] High defect content crystals have been recently reported such as the d-MAPI class of materials with general formula $(A)_{1-2.48x}(B)_{3.48x}[M_{1-x}I_{3-x}]$ (A = MA, FA; B = hydroxyethylammonium (HEA^+), thioethylammonium (TEA^+), 1,2,4-triazolium (TzH^+); $M = Pb^{2+}$, Sn^{2+})[24-27] and the "hollow" halide perovskites with general formula $(A)_{1-x}(B)_x(M)_{1-0.7x}(I)_{3-0.4x}$ (A = MA, FA; B = ethylenediammonium (*en*), propylenediammonium (PN) and trimethylenediammonium (TN); $M = Pb^{2+}$, Sn^{2+}).[28-31] In both of these families, the introduction of A site cations longer than MA and FA, such as for example, *en*, HEA and TEA, cause the removal of metal halide moieties from the crystal lattice generating vacancy defects in the 3D framework. In the case of d-MAPI materials, the structure consists of a 3D corner sharing perovskite $Pb_{1-x}I_{3-x}$ (x = 0 to 0.20) lead and iodide-deficient 3D network of periodically localized defects. On the contrary, in the case of "hollow" perovskites the lead and iodide defects are randomly

dispersed in the crystal structure, giving rise to the archetype cubic 3D perovskite network.

A striking attribute of these vacancy defect materials is the systematic alteration of the optical properties, in proportion to the number of defects in the crystal structure. For example, in the "hollow" $(MA)_{1-x}(en)_x(Pb)_{1-0.7x}(I)_{3-0.4x}$ compounds, the bandgap can be adjusted from 1.52 eV for pristine $MAPbI_3$ (x = 0) to 2.1 eV for the $(MA)_{0.56}(en)_{0.44}(Pb)_{0.692}(I)_{2.824}$ (x = 0.44) analog. Unlike the pristine perovskites, the "hollow" versions adopt the high symmetry cubic α phase ($SrTiO_3$)[32-33]. In addition, they are considerably more environmentally stable. For example, the $(MA)_{1-x}(en)_x(Sn)_{1-0.7x}(I)_{3-0.4x}$ family of perovskites are two orders of magnitude (16 days in air for the 40% *en* based sample) long lived than the pristine $MASnI_3$ (x = 0) , which is stable in air for less than 10 min, while the Pb analogs of "hollow" perovskites are stable for almost a year compared to hours-to-weeks of stability reported for pristine α-$FAPbI_3$ and β-$MAPbI_3$ compositions.[29]

We were intrigued by the environmental stability and optoelectronic properties of the "hollow" perovskites, and whether the Pb bromide perovskites could form "hollow" structures. Given the smaller size of the 3D cage in the bromine analogs compared to the iodine analogs, we wanted to determine if such structures can form at all and if so, how would they compare and contrast to the iodides. Here, we report a new family of defective materials with general formula $(FA)_{1-x}(en)_x(Pb)_{1-0.7x}(Br)_{3-0.4x}$ (FA = formamidinium, *en* = ethylenediammonium, x = 0-0.44). This is the first demonstration of engineering bromide perovskites with tunable defects in single crystal form, while recently Worku et al. reported "hollow" $CsPbBr_3$ nanoparticles.[34] Using single crystal X-ray diffraction and PDF analysis we show the defective nature of the materials deriving from the replacement of Pb atoms by *en* dications. In particular, we employed solid state NMR spectroscopy to shed light on the local structural environment of *en* molecules revealing the presence of two types of defects in the crystal lattice. The optical properties can be fine-tuned by controlling the degree of *en* molecule incorporation. Usually the presence of structural defects act as non-radiative recombination centers (traps) and quenches PL emission.[35] Surprisingly, we observed that above 40% *en* incorporation there is strong broad light emission centered at 590 nm, with 1% PLQY at room temperature (RT), which is tunable in intensity by controlling the content of *en* in the lattice. Although, broad light emission is common for low dimensional perovskites and metal halides,[36-38] the emission performance of the

"hollow" bromide compounds is unique and noteworthy among 3D hybrid halide perovskites.[39-41]

RESULTS AND DISCCUSSION

Synthetic aspects and structural characterization

High quality single crystals of $(FA)_{1-x}(en)_x(Pb)_{1-0.7x}(Br)_{3-0.4x}$ (x = 0, 0.7, 0.18, 0.29, 0.40, 0.42, 0.44) were synthesized by dissolving lead (II) acetate, formamidinium acetate and various amounts of ethylenediamine (maximum nominal ratio of *en*:FA:Pb: = 1:1:1) in a hot acidic H_3PO_2/HBr solvent mixture (Figure S1). Due to the excess of A site cations present in the solution at *en*:Pb ratios (0.5-1:1), the corresponding crystals must be isolated from the mother solution shortly after formation to avoid the coprecipitation of the non-perovskite phase $(en)_2PbBr_6$ upon cooling. The existence of $(en)_2PbBr_6$ was confirmed by single crystal X-ray diffraction (XRD) analysis (Tables S1-5). The structure was reported previously by Lemmerer et al. and consists of 1D ribbons of corner-sharing $[PbBr_6]^{4-}$ octahedra separated by ethylenediammonium cations and free bromide anions, that charge balance the structure (more precisely $[(H_3NC_2H_4NH_3)_4Pb_2Br_9 \cdot 3Br^-]$).[42]

Powder X-ray diffraction (PXRD) measurements verified the phase purity of the as made single crystals, and confirmed they are all isostructural to the pristine cubic α-$FAPbBr_3$ (Figures 1, S2-3). Notably with increasing amount of *en* in the structure there is a gradual unit cell expansion which is clear from the shift of the PXRD patterns to lower 2θ values. The pristine and hollow samples (0, 0.18, 0.29, 0.42 content of *en*) crystallize at the same cubic *Pm*-3*m* space group (Table 1). At the same time even at high *en* loading (44%), the structure retains its 3D dimensionality (Figure S4). All structures were solved and refined using single crystal X-ray diffraction measurements. However, the locations of *en* cations could not be crystallographically resolved because of the lack of periodicity and nonuniform distribution in the crystal lattice, displacing FA^+, Pb^{2+}, and Br^- ions, thus creating a large number of defects (Figure 2). The only pronounced difference among the solved crystal structures is the elongation of the Pb-Br bonds, from 2.9963(3) Å to 3.03200(10) Å giving rise to a unit cell volume expansion from 215.202(19) $Å^3$ to 222.986(6) $Å^3$ for the pristine and 42% *en* sample

accordingly (Figure 3 and Tables 2, S6-S21). Imposed by the cubic *Pm*-3*m* space group all Pb-Br-Pb angles are 180 deg.

Occupancy refinement of the Pb and Br atom sites revealed that by increasing the content of *en* in the structure, there is a rising number of Pb and Br atom vacancies, which is significantly more pronounced for the heavy Pb atoms (up to 20% for 42% *en* incorporation) (Table S22). This was further supported by energy dispersive spectroscopy (EDS) measurements where for the 42% *en* sample the ratio of Pb:Br is 1:3.9 instead of 1:3 (Figure S5). Thermogravimetric (TGA) analysis corroborates the above results. By increasing the amount of incorporated *en* there is a gradual weight loss increase in the first step of the graph, which corresponds to FABr and *en*Br_2 loss at around 300 °C. This weight loss change ranges from 25.1% to 36.2% for the pristine and 42% *en* based materials respectively (Figures S6-S9). At the same time, the mass loss at the second step at around 430 °C corresponds to the removal of the $PbBr_2$ inorganic part, which decreases gradually from 73.4% to 60.5% for the pristine and 42% *en* based materials respectively. These results confirm the reduction in the amount of Pb with increasing amount of *en* in the structure (Table S23).

Solution ^{1}H-NMR spectroscopy measurements verified the presence of *en* in the crystal structure and the ratio among *en* and FA cations. The quantification was based on both the methine (=CH-, δ = 7.87 ppm) and the ammonium (-NH_2^+, δ = 8.69 ppm, 9.03 ppm) protons of the FA cation versus the methylene (-CH_2-, δ = 3.07 ppm) and the ammonium (-NH_3^+, δ = 7.89 ppm) protons of the *en* cations. In FA, the integration of those peaks reveals a ratio of 2:2:1, since there is one proton from the methine group (=CH-) and four protons from the two amine cations (-NH_2^+). In *en*, the ratio of the 2 peaks is 4:6, arising from four -CH_2- protons and six ammonium (-NH_3^+) protons, suggesting that *en* is doubly protonated.

Experimental crystal densities determined from a commercially available pycnometer indicated that the density of the samples decreases proportionally to *en* incorporation in the structure from 3.8116(1) cm^3 g^{-1} to 3.4657(1) cm^3 g^{-1} for the pristine and 42% *en* sample accordingly (Table S24). This trend is further supported by the observed expansion of the unit cell dimensions with increasing *en* content, coupled with reduced site occupancies of the heavy atoms which further lowers crystal density.

Considering the disordered nature of the corresponding “hollow” materials, which do not allow direct structure determination as in the case of ordered defective d-

$MAPbI_3$ analogs,[25] an indirect method was designed for the assembly of a representative chemical formula that can describe efficiently the hollow compounds. In order to examine whether the formula of the hollow iodide samples $(A)_{1-x}(en)_x(M)_{1-0.7x}(I)_{3-0.4x}$, can be applied in the bromide analogs as well, we followed a previously established analysis protocol,[29] combining the data from four different characterization techniques, ^{1}H-NMR, PXRD, XRD, and crystal density measurements. In particular, we compared the theoretical crystal density derived from the examined formula with the experimental crystal density obtained from single-crystal XRD and pyncometry measurements (Table S24), and good agreement is obtained betweenexperimental and the calculated ones based on PXRD and ^{1}H-NMR studies (0.4-4% difference in crystal density values). The values derived from the pycnometry studies have showed somewhat higher variation than the theoretical ones in the range from 0.07% for the pristine material to 8% for the 42% *en* sample. In addition, the EDS results for the highly hollow sample, $(FA)_{0.58}(en)_{0.42}(Pb)_{0.706}(Br)_{2.832}$ gave a Pb:Br ratio of 1:3.9 which is close to the 1:4 ratio deriving from the formula. Based on these results, we propose the molecular formula $(FA)_{1-x}(en)_x(Pb)_{1-0.7x}(Br)_{3-0.4x}$ to describe the chemical composition of the "hollow" bromide analogs. For simplicity purposes the notation % *en*/$FAPbBr_3$ will be used throughout this work.

The unit cell volume expansion, reduction in the crystal density and the associated blue shift in the absorption and emission spectra (see below) are proportional to *en* incorporation, which is a characteristic to hollow perovskites. Another feature of the "hollow" bromide perovskites (similar to the iodides) is the change in the crystal morphology, from rhombic dodecahedral shape for the pristine material $FAPbBr_3$ to regular octahedral for the "hollow" bromide crystals, is attained from scanning electron microscopy (SEM) measurements (Figure 4) and analysis.

Structural phase transitions. A well-known characteristic of all perovskite structures is the phase transitions associated with the behaviour of the metal octahedra tilting as a function of temperature. Using high resolution variable temperature PXRD studies using synchrotron radiation, for the first time we shed light on the phase transitions occurring in both "hollow" iodide and bromide perovskites. We find that *en* incorporation can suppress temperature dependent phase transitions. The "hollow" bromide samples are stable in the cubic α-phase over a wide range of temperatures (94K-493K) (Figures 5, S16). The thermal stability and robustness of the hollow perovskite structure up to 493 K is accompanied by a gradual increase of the unit cell

dimensions due to thermal expansion (from 6.02082(1) Å at 94K to 6.13381(2) Å at 493K for the 42% *en* material), which is a norm for hybrid perovskites and metal halide materials.[36, 43] For example, pristine $FAPbBr_3$ exhibits two distinct phase transitions in this temperature range. One between 275 and 250 K, giving rise to a tetragonal *P*4/*mbm* phase, while upon further cooling, the structure distorts more giving rise to an orthorhombic *Pnma* phase between 150 and 125 K.[44]

The same behavior is observed for the corresponding "hollow" $MAPbI_3$ and $FAPbI_3$ samples. Both 33% *en*/$MAPbI_3$ and 40% *en*/$FAPbI_3$ crystallize at the cubic *Pm*-3*m* space group over the entire examined temperature range as the hollow $FAPbBr_3$ compounds (Figures S17-18). On the contrary, pristine $MAPbI_3$ crystals exhibit two phase transitions, one at ~330 K, from cubic α (*Pm*-3*m*) to tetragonal β (*I*4/*mcm*) and one at ~160 K, from tetragonal to orthorhombic (*Pnma*).[45-46] Pristine cubic $FAPbI_3$ crystals exhibit poor environmental stability for a long time period (from min up to 8 days depending on heat treatment).[29] The material's temperature profile is governed by two distinct structural phase transitions, one at ~ 285 K, from cubic α (*Pm*-3*m*) to tetragonal β (*P*4/*mbm*) and one at ~ 140 K, from tetragonal β (*P*4/*mbm*) to tetragonal γ (*P*4/*mbm*).[47-48] Simenas et.al. reported a similar trend in the case of $MA_{1-x}DMA_xPbBr_3$ single crystals and observed significant suppression of the structural phase transitions, stabilization of the cubic phase and disorder even for a small amount of dimethylammonium cations.[49] The stabilization of a cubic high temperature phase at lower temperatures due to the presence of defects and increased structural disorder is a well-known phenomenon in metal oxides as well.[50-51]

Local structure through pair distribution function analysis. Pair distribution function (PDF) analysis was utilized to shed light on the local crystal structure of the materials. This method is specifically adopted for the characterization of disordered compounds with limited structural coherence.[52-54] The goal of this study was to identify significant deviations from the average crystal structure that may be present and caused by the FA/*en* disorder and Pb/Br vacancies in the lattice. The PDF data confirm the increase in unit cell volume from 216 $Å^3$ in $FAPbBr_3$ to 222 $Å^3$ in the hollow $FAPbBr_3$ samples found by the conventional XRD studies mentioned above. Qualitative comparison of the PDF for pristine $FAPbBr_3$ and 40% *en* substituted $FAPbBr_3$ (Figure 6a) demonstrates a decrease in the number of several pair correlations with *en* substitution, suggesting a smaller concentration of strong scatterers. Several pair

correlations also show tailing on the high *r* side of the peak indicating an asymmetric increase in the distribution of Pb-Br bond distances. Fitting of the PDF to the average cubic perovskite structure (*Pm*-3*m*) indicates that the reduction in intensity and tailing originates primarily from changes at the Pb site. This is most clearly observed by comparing the partial PDFs calculated for Br-Br pair correlations and Pb-Pb pair correlations (Figure 6b). The Br-Br correlations are visually quite similar between the pristine and "hollow" samples. In contrast, Pb-Pb pair correlations exhibit marked decreases in intensity and increase in peak tailing between the pristine and "hollow" perovskite similar to that observed in the total PDF. These features are accompanied by a reduction in the refined Pb site occupancy from 1.02 in pristine $FAPbBr_3$ to 0.85 for 40% *en* substituted $FAPbBr_3$, which is consistent with the results from the single crystal XRD studies. The PDF data therefore demonstrate that *en* substitution leads to decreased Pb atom occupancy, increased disorder and increased Pb-Br bond distances.

Elucidation of short-range structures and interactions through solid-state NMR spectroscopy. Short-range structures of *en* cations in the $FAPbBr_3$ perovskite framework are best consolidated by solid-state NMR spectroscopy measurements and analysis. For example, ssNMR spectroscopy has recently been applied to characterize local structures and intermolecular interactions in optoelectronic materials. Figure 7 compares 1D and 2D ^{1}H ssNMR spectra of enI, $FAPbBr_3$ and *en* substituted $FAPbBr_3$ at different stoichiometric concentrations, whereby signals correspond to distinct ^{1}H sites, 4.1 (CH_2, *en*), 7.5 (NH_2, *en*, FA^+) and 8.1 ppm (CH, FA^+) are color coded as depicted in the schematic structures. Of particular interest is the narrow ^{1}H signals (~4.1 ppm) indicate that the *en* cations are incorporated into the $FAPbBr_3$ framework, compared to broad distributions of signals (3-4 ppm) in the case of *en*I salt that originate from strong dipole-dipole interactions between neighboring *en* molecules. In addition, deconvolution ^{1}H NMR spectra of 12% *en*, 33% *en* and 44% *en* suggests that the *en* dispersion in $FAPbBr_3$ reaches to a saturation point at ~29% *en*, and higher loadings of *en* yield to cation aggregation: 33% *en* and 41% *en* loaded $FAPbBr_3$ results in ~5% and 12% of *en* cations to aggregate leading to broad signals in their ^{1}H NMR spectra (Figure 7a, inset). Distribution of *en* cations in the perovskite framework is further corroborated by analysing 2D ^{1}H-^{1}H double-quantum (DQ) and ^{1}H-^{1}H spin-diffusion spectra of 41% *en* $FAPbBr_3$. The DQ signals can be excited for inter- and intramolecular dipolar coupled H···H pairs at sub-nanometer distances <0.5 nm (Figure 7b): the on-diagonal

DQ signals at 8.2 ppm correspond to H···H proximities in CH_2 groups of *en* and a broad feature at ~15 ppm corresponds to overlapped signals associated with NH_2 groups in *en* and FA^+. The off-diagonal DQ signal at 11.6 ppm corresponds to H···H proximities between chemically distinct CH_2 and NH_2 groups of *en*, and at 15.8 ppm is due to through-space proximities between CH and NH_2 groups of FA^+. Notably, ^{1}H DQ peaks between -CH- groups of FA^+ and -CH2- groups of *en* (red arrow) indicates the through-space close proximity (<0.5 nm) between -CH- (FA^+) and -CH_2- (*en*), confirming the presence of *en* cations in the perovskite framework.

To gain further insight into the local structures of organic cations in 41% *en* $FAPbBr_3$, 2D ^{1}H-spin diffusion spectra were analyzed and compared. In a spin diffusion experiment, magnetization is allowed to exchange between ^{1}H sites as a function of mixing time. In the case of 41% *en* $FAPbBr_3$, shorter mixing times (<20 ms) allow the ^{1}H spin magnetization exchange within the same cations, and longer mixing times (>50 ms) allowed the ^{1}H magnetization exchange between *en* and FA^+ cations (red arrows), as depicted in Figure 7c and Figure S19 (Supporting Information). Overall, 2D ssNMR experiments further corroborate the XRD and PDF results and analysis, and provide an atomic-level picture of local chemical environments of *en* in the $FAPbBr_3$ perovskite.

Optical absorption, photoluminescence and work functions

All compounds exhibit sharp optical absorption edges based on diffuse reflectance measurements, while the band gap blue shifts from 2.20 eV for the pristine $FAPbBr_3$, to 2.60 for the 42% *en* one (Figure 8a and Table 2). This is accompanied by a crystal color change from orange to yellow. The removal of Pb-Br fragments from the crystal structure, leads to discontinuities in the infinite Pb-Br-Pb connectivity in the 3D lattice which reduces the degree of orbital overlap between these atoms preventing the development of the full possible electronic band width. This results in widening of the bandgap with increasing amount of *en*. Large bandgap widening in perovskites is only possible through dimensional reduction which gives rise to the various classes of two-dimensional compounds such as the Ruddlesden-Popper (RP),[55-56] the Dion-Jacobson (DJ)[57-58] and the alternating cation in the interlayer space (ACI) type.[59] The achievement of "hollow" structures presents a second mode of widening the bandgap while keeping the overall dimensionality 3D. This phenomenon can be exploited to

precisely tune the band gap of the 3D structure by controlling the incorporation of *en* cations.

The "hollow" bromide perovskite materials exhibit strong narrow band edge PL emission which correlates to the amount of incorporated *en* in the crystal structure, spanning from 543 nm for pristine $FAPbBr_3$, to 480 nm for the 29% *en* sample (Figure 8b). However, a surprising change in behavior was observed when the incorporation of *en* exceeded 29%. Apparently above 29% the PL peak broadens significantly, and for 40% *en* loading, there is very strong broad light emission centered at 590 nm. The intensity is enhanced further by increasing the amount of *en*, for up to 44% *en* loading where it saturates (Figure S20). This is a clear and rare example of the manipulation of the strength of the PL emission of halide perovskites by defect engineering.[60-62]

The optical properties of the 42% *en* sample were examined in detail and are presented below. Upon excitation of the crystals with a 380 nm beam, 42% *en* sample exhibits a broad strong emission centered at 590 nm with a large full width at half maximum (FWHM) of 195 nm (0.67 eV) accompanied by a large energy shift of 110 nm (0.48 eV) (Figure 9a). The corresponding determined PLQY is 1%, while the PL peak position and FWHM is the same regardless of excitation power (Figure S22). This performance (strong broad light emission at RT) is unique among 3D hybrid halide perovskites. The only reports of stronger PL emission from 3D halide perovskites are based on 3D perovskite films, e.g. $MASnI_3$ and $CsSnI_3$ with narrow band edge emission[39-40] and 3D fully inorganic double perovskite $Cs_2(Ag_{0.60}Na_{0.40})InCl_6$ with strong broad emission.[63] Additionally, this is a clear demonstration of not only the high defect tolerance of the corresponding materials but also the ability to utilize defects to tailor the optoelectronic properties of these systems. Furthermore, the intensity and line shape of the PL emission of the 42% *en* compound is maintained after exposure of the perovskite in air for a year, demonstrating the excellent structural stability and integrity of the emission performance of this defective material (Figure S21). We should point out that such robust emission is among the highest reported for halide perovskite materials.[64] The excellent air stability of the "hollow" perovskites may be ascribed to suppressed ion migration, by the presence of a large amount of *en* dications in the lattice. This is supported by our recent work, examining the electronic and ionic conductivity in the "hollow" $MAPbI_3$ system. The suppression of ion migration is

reflected by the significant increase of the activation energies for iodide ion migration with higher *en* content derived from both experimental data and ab initio simulations.

The corresponding CIE (International Commission on Illumination) chromaticity coordinates for the 42% *en* compound are (0.47, 0.49), with a much larger contribution from the red region of the spectrum as compared to pure white light, which has chromaticity coordinates of (0.33, 0.33). This broad emission is described by a correlated color temperature (CCT) of 3144 K (warm yellow light), and a color-rendering index (CRI) value of 67, meaning that this light is suitable for outdoor lighting (Figure 10c and Table 3). CIE coordinates and CCT values were calculated using the ColorCalculator by OSRAM Sylvania, Inc. CRI index quantifies how accurately illuminated colors are reproduced; for indoor lighting values above 80 are required.[65]

Interestingly, the emission performance of the "hollow" bromide materials is very different from the case of the iodide analogs, where with increasing amount of *en* the PL quenches above 35% *en* loading.[29] It has been shown that 3D iodide perovskite analogs have a lower bulk modulus than bromide perovskites and are therefore softer and more prone to distortion,[66] a trait linked to weaker electron-phonon coupling and lower polaron binding energy for the iodide analogs.[67-68] It is possible that for highly defective systems the latter characteristics are enhanced, generating transient lattice deformations that act as non-radiative recombination centers for the softer iodide lattice, and as radiative recombination centers (in the form of self-trapped excitons (STEs)) for the stiffer bromide lattice (see below).

Determination of the electronic band energies of the corresponding "hollow" bromide compounds was realized by performing photoemission yield spectroscopy in air (PYSA) measurements.[69] The position of the valence band maxima (VBM) was determined through PYSA measurements, while the conduction band minima (CBM) was determined by subtracting the corresponding optical band gap values from the measured VBM energies (Figure S23). Apparently with increasing amount of *en* in the structure the VBM of the hollow materials moves lower in energy, from 5.62 eV in the pristine $FAPbBr_3$ to 5.78 eV for the 42% *en* sample. Notably the later value is very close to the 2D and 1D lead bromide compounds, such as $(2,6\text{-dmpz})_3Pb_2Br_{10}$ with strong broad light emission (12% PLQY).[70] This finding coupled with the blue shift of the energy bandgaps supports the view that the electronic character of the hollow 3D materials is less than 3D and closer to low dimensional compounds.

Origin of PL emission

In order to learn more about the mechanism of the broad emission, variable-temperature PL measurements were performed from 80 to 300K (Figure 9b). With decreasing temperature there is a gradual increase in the broad emission intensity up to 180 K with no change in the PL lineshape. At 160K a new narrow PL peak (FWHM 10.4 nm) appears centered at 498 nm (2.49 eV) accompanied by an increase of the PL intensity by one order of magnitude for both the narrow and the broad PL peaks. The narrow emission is significantly enhanced in intensity as compared to the broad emission by lowering the temperature down to 80K, (FWHM 12.2 nm) without any recorded shift in the emission wavelength for both peaks (Figure S24). This behavior is typical for broad light emitters with energy barrier to be crossed from the free exciton (FE), to STE states.[71-72] At RT, the thermal energy is large compared to this barrier and the broad emission from STEs is dominant. At lower temperature, some FEs cannot cross the energy barrier and hence a narrow FE emission, increasing exponentially with lowering the temperature, appears at higher energy.[70, 72-73]

The measured average decay lifetime at RT was 15 ns, determined using multi-exponential fitting of the emission decay curve (Figure 9c), showing three components with decay constants of 1.6, 10.2 and 22.2 ns. At 80 K the STE lifetime (measured at 575 nm) shows a fast component followed by a slow single exponential decay with lifetime of 130 ns. Notably, at RT the recorded lifetime is comparable to QD (Quantum dot) materials, with values of few ns,[74] as in the case of the "hollow' $CsPbBr_3$ nanocrystals,[34] 1D strong light emitting metal halide materials, such as $C_4N_2H_{14}PbBr_4$ with recorded values of few tens of ns,[75] and 2D white light emitters such as $[(C_6H_5C_2H_4NH_3)_2PbCl_4]$ with values of a few ns as well.[76]

Power dependent PL studies (up to 900 mW cm^{-2}) indicate a linear correlation between the PL intensity and the excitation power density. This suggests that the emission stems from self-trapped excitons (STEs) (Figure 9d)[77-79] and not permanent defects, where the PL emission saturates at higher excitation power.[17, 36, 80]

High temperature measurements (300K to 460 K) (Figure S25) indicate no change in the PL line shape and emission wavelength. However, above 300 K the PL emission decreases in intensity gradually up to 460 K. It is well demonstrated that the PL intensity in disordered semiconductors, decreases dramatically with increasing

temperature due to the increased nonradiative recombination of thermally delocalized carriers.[81-82]

CONCLUSIONS

Significant amounts of *en* can be incorporated in the crystal structure of $FAPbBr_3$ without causing a structural transformation to a two-dimensional material. The size of the *en* cation is considered too large and outside the scope of the so-called Goldsmith tolerance factor to be incorporated in a perovskite cage. However, because of the creation of massive vacancies by Pb and Br atoms, adjacent cages can fuse to become larger cages effectively making the Goldsmith tolerance factor irrelevant. Taking advantage of this chemical versatility of hybrid perovskites we created a new class of "hollow" 3D hybrid halide perovskites with general formula $(FA)_{1-x}(en)_x(Pb)_{1-0.7x}(Br)_{3-0.4x}$, x = 0-0.44 where *en* cations induced randomly dispersed vacancy defects in the lattice by replacing Pb, Br and FA moieties. Solid state NMR studies suggest the *en* cations are well dispersed into the perovskite framework at *en* loadings less than 30%, whereas two types of local chemical environments of *en* molecules are observed at *en* loadings greater than 30%. By manipulating the amount of incorporated *en* dications the optical properties of the corresponding crystals can be fine-tuned over a wide energy range both in terms of emission and absorption spectra. Above 40% *en* inclusion, the hollow bromide perovskite emits strong broad light at RT which is directly correlated to the number of defects, increasing gradually in intensity for 42%, and reaching a plateau at 44% *en*, with 1% PLQY coupled with a lifetime of 15 ns. The corresponding material maintains its strong PL emission after one-year air exposure. This is the first time that strong broad light emission from a 3D hybrid halide perovskite is observed, while its PL robustness under ambient conditions is among the highest reported for halide perovskites.

ASSOCIATED CONTENT

Supporting Information

Materials and methods, synthetic details, additional supplementary figures and tables about material characterization, X-ray diffraction measurements, photoluminescence measurements, thermogravimetric analysis, NMR, XRF, EDS and PYSA measurements.

This material is available free of charge via the Internet at http://pubs.acs.org.

AUTHOR INFORMATION

Corresponding Authors

m-kanatzidis@northwestern.edu

Present address

[#]Department of Chemical and Environmental Engineering, Yale University, 9 Hillhouse Avenue, New Haven, CT 06520, USA

Notes

The authors declare no competing financial interest.

ACKNOWLEDGMENT

This work is primarily supported by the Department of Energy, Office of Science, Basic Energy Sciences, under Grant No. SC0012541 (sample synthesis, structure and property characterization). This work made use of the SPID, and EPIC facilities of Northwestern University's NU*ANCE* Center, as well as the IMSERC facilities, which have received support from the Soft and Hybrid Nanotechnology Experimental (SHyNE) Resource (NSF ECCS-1542205); the MRSEC program (NSF DMR-1720139) at the Materials Research Center, from the State of Illinois, and the International Institute for Nanotechnology (IIN). This work was performed, in part, at the Center for Nanoscale Materials, a U.S. Department of Energy Office of Science User Facility, and supported by the U.S. Department of Energy, Office of Science, under Contract No. DE-AC02-06CH11357.

REFERENCES

1. Stoumpos, C. C.; Kanatzidis, M. G., The Renaissance of Halide Perovskites and Their Evolution as Emerging Semiconductors, *Acc. Chem. Res.* **2015,** *48*, 2791-2802.
2. Stoumpos, C. C.; Kanatzidis, M. G., Halide Perovskites: Poor Man's High-Performance Semiconductors, *Adv. Mater.* **2016,** *28*, 5778-5793.
3. Berry, J.; Buonassisi, T.; Egger, D. A.; Hodes, G.; Kronik, L.; Loo, Y.-L.; Lubomirsky, I.; Marder, S. R.; Mastai, Y.; Miller, J. S.; Mitzi, D. B.; Paz, Y.; Rappe, A. M.; Riess, I.; Rybtchinski, B.; Stafsudd, O.; Stevanovic, V.; Toney, M. F.; Zitoun, D.; Kahn, A.; Ginley, D.; Cahen, D., Hybrid Organic–Inorganic Perovskites (HOIPs): Opportunities and Challenges, *Adv. Mater.* **2015,** *27*, 5102-5112.
4. Manser, J. S.; Christians, J. A.; Kamat, P. V., Intriguing Optoelectronic Properties of Metal Halide Perovskites, *Chem. Rev.* **2016,** *116*, 12956-13008.

5. Chen, K.; Schünemann, S.; Song, S.; Tüysüz, H., Structural effects on optoelectronic properties of halide perovskites, *Chem. Soc. Rev.* **2018,** *47*, 7045-7077.
6. Saparov, B.; Mitzi, D. B., Organic–Inorganic Perovskites: Structural Versatility for Functional Materials Design, *Chem. Rev.* **2016,** *116*, 4558-4596.
7. Chouhan, L.; Ghimire, S.; Subrahmanyam, C.; Miyasaka, T.; Biju, V., Synthesis, optoelectronic properties and applications of halide perovskites, *Chem. Soc. Rev.* **2020,** *49*, 2869-2885.
8. Koji, Y.; Hiroshi, K.; Takashi, M.; Tsutomu, O.; Sumio, I., Structural Phase Transition and Electrical Conductivity of the Perovskite $CH_3NH_3Sn_{1-x}Pb_xBr_3$ and $CsSnBr_3$, *Bull. Chem. Soc. Jpn.* **1990,** *63*, 2521-2525.
9. Stoumpos, C. C.; Malliakas, C. D.; Kanatzidis, M. G., Semiconducting Tin and Lead Iodide Perovskites with Organic Cations: Phase Transitions, High Mobilities, and Near-Infrared Photoluminescent Properties, *Inorg. Chem.* **2013,** *52*, 9019-9038.
10. MØLler, C. K., Crystal Structure and Photoconductivity of Cæsium Plumbohalides, *Nature* **1958,** *182*, 1436-1436.
11. Zhao, D.; Yu, Y.; Wang, C.; Liao, W.; Shrestha, N.; Grice, C. R.; Cimaroli, A. J.; Guan, L.; Ellingson, R. J.; Zhu, K.; Zhao, X.; Xiong, R.-G.; Yan, Y., Low-bandgap mixed tin–lead iodide perovskite absorbers with long carrier lifetimes for all-perovskite tandem solar cells, *Nat. Energy* **2017,** *2*, 17018.
12. Stranks, S. D.; Eperon, G. E.; Grancini, G.; Menelaou, C.; Alcocer, M. J. P.; Leijtens, T.; Herz, L. M.; Petrozza, A.; Snaith, H. J., Electron-Hole Diffusion Lengths Exceeding 1 Micrometer in an Organometal Trihalide Perovskite Absorber, *Science* **2013,** *342*, 341-344.
13. Dong, Q.; Fang, Y.; Shao, Y.; Mulligan, P.; Qiu, J.; Cao, L.; Huang, J., Electron-hole diffusion lengths > 175 μm in solution-grown $CH_3NH_3PbI_3$ single crystals, *Science* **2015,** *347*, 967-970.
14. Wei, H.; Huang, J., Halide lead perovskites for ionizing radiation detection, *Nat. Commun.* **2019,** *10*, 1066.
15. Kanaya, S.; Kim, G. M.; Ikegami, M.; Miyasaka, T.; Suzuki, K.; Miyazawa, Y.; Toyota, H.; Osonoe, K.; Yamamoto, T.; Hirose, K., Proton Irradiation Tolerance of High-Efficiency Perovskite Absorbers for Space Applications, *J. Phys. Chem. Lett.* **2019,** *10*, 6990-6995.
16. Reb, L. K.; Böhmer, M.; Predeschly, B.; Grott, S.; Weindl, C. L.; Ivandekic, G. I.; Guo, R.; Dreißigacker, C.; Gernhäuser, R.; Meyer, A.; Müller-Buschbaum, P., Perovskite and Organic Solar Cells on a Rocket Flight, *Joule* **2020,** *4*, 1880-1892.
17. Meggiolaro, D.; Motti, S. G.; Mosconi, E.; Barker, A. J.; Ball, J.; Andrea Riccardo Perini, C.; Deschler, F.; Petrozza, A.; De Angelis, F., Iodine chemistry determines the defect tolerance of lead-halide perovskites, *Energy Environ. Sci.* **2018,** *11*, 702-713.
18. Chu, W.; Zheng, Q.; Prezhdo, O. V.; Zhao, J.; Saidi, W. A., Low-frequency lattice phonons in halide perovskites explain high defect tolerance toward electron-hole recombination, *Sci. Adv.* **2020,** *6*, eaaw7453.
19. Kim, G.-W.; Petrozza, A., Defect Tolerance and Intolerance in Metal-Halide Perovskites, *Adv. Energy Mater.* **2020,** *10*, 2001959.
20. Kumar, S.; Hodes, G.; Cahen, D., Defects in halide perovskites: The lattice as a boojum?, *MRS Bull.* **2020,** *45*, 478-484.
21. Yin, W.-J.; Shi, T.; Yan, Y., Superior Photovoltaic Properties of Lead Halide Perovskites: Insights from First-Principles Theory, *J. Phys. Chem. C* **2015,** *119*, 5253-5264.
22. Huang, J.; Yuan, Y.; Shao, Y.; Yan, Y., Understanding the physical properties of hybrid perovskites for photovoltaic applications, *Nat. Rev. Mater.* **2017,** *2*, 17042.
23. Sun, C.; Xu, L.; Lai, X.; Li, Z.; He, M., Advanced Strategies of Passivating Perovskite Defects for High-Performance Solar Cells, *Energy Environ. Mater.* **2020,** *n/a*.
24. Leblanc, A.; Mercier, N.; Allain, M.; Dittmer, J.; Pauporté, T.; Fernandez, V.; Boucher, F.; Kepenekian, M.; Katan, C., Enhanced Stability and Band Gap Tuning of α-$[HC(NH_2)_2]PbI_3$ Hybrid Perovskite by Large Cation Integration, *ACS Appl. Mater. Interfaces* **2019,** *11*, 20743-20751.
25. Leblanc, A.; Mercier, N.; Allain, M.; Dittmer, J.; Fernandez, V.; Pauporté, T., Lead- and Iodide-Deficient $(CH_3NH_3)PbI_3$ (d-MAPI): The Bridge between 2D and 3D Hybrid Perovskites, *Angew. Chem. Int. Ed.* **2017,** *56*, 16067-16072.
26. Tsai, C.-M.; Lin, Y.-P.; Pola, M. K.; Narra, S.; Jokar, E.; Yang, Y.-W.; Diau, E. W.-G., Control of Crystal Structures and Optical Properties with Hybrid Formamidinium and 2-Hydroxyethylammonium Cations for Mesoscopic Carbon-Electrode Tin-Based Perovskite Solar Cells, *ACS Energy Lett.* **2018,** *3*, 2077-2085.
27. McNulty, J. A.; Slawin, A. M. Z.; Lightfoot, P., Variable dimensionality in 'hollow' hybrid tin iodide perovskites, *Dalton Trans.* **2020,** *49*, 15171-15174.

28. Ke, W.; Stoumpos, C. C.; Zhu, M.; Mao, L.; Spanopoulos, I.; Liu, J.; Kontsevoi, O. Y.; Chen, M.; Sarma, D.; Zhang, Y.; Wasielewski, M. R.; Kanatzidis, M. G., Enhanced photovoltaic performance and stability with a new type of hollow 3D perovskite {en}FASnI$_3$, *Sci. Adv.* **2017,** *3*, e1701293.
29. Spanopoulos, I.; Ke, W.; Stoumpos, C. C.; Schueller, E. C.; Kontsevoi, O. Y.; Seshadri, R.; Kanatzidis, M. G., Unraveling the Chemical Nature of the 3D "Hollow" Hybrid Halide Perovskites, *J. Am. Chem. Soc.* **2018,** *140*, 5728-5742.
30. Ke, W.; Stoumpos, C. C.; Spanopoulos, I.; Chen, M.; Wasielewski, M. R.; Kanatzidis, M. G., Diammonium Cations in the FASnI3 Perovskite Structure Lead to Lower Dark Currents and More Efficient Solar Cells, *ACS Energy Lett.* **2018,** *3*, 1470-1476.
31. Ke, W.; Spanopoulos, I.; Tu, Q.; Hadar, I.; Li, X.; Shekhawat, G. S.; Dravid, V. P.; Kanatzidis, M. G., Ethylenediammonium-Based "Hollow" Pb/Sn Perovskites with Ideal Band Gap Yield Solar Cells with Higher Efficiency and Stability, *J. Am. Chem. Soc.* **2019,** *141*, 8627-8637.
32. Abramov, Y. A.; Tsirelson, V. G.; Zavodnik, V. E.; Ivanov, S. A.; Brown I. D., The chemical bond and atomic displacements in $SrTiO_3$ from X-ray diffraction analysis, *Acta Crystallogr. Sect. B* **1995,** *51*, 942-951.
33. Cowley, R. A., Lattice Dynamics and Phase Transitions of Strontium Titanate, *Phys. Rev.* **1964,** *134*, A981-A997.
34. Worku, M.; Tian, Y.; Zhou, C.; Lin, H.; Chaaban, M.; Xu, L.-j.; He, Q.; Beery, D.; Zhou, Y.; Lin, X.; Su, Y.-f.; Xin, Y.; Ma, B., Hollow metal halide perovskite nanocrystals with efficient blue emissions, *Sci. Adv.* **2020,** *6*, eaaz5961.
35. Liu, X.-K.; Xu, W.; Bai, S.; Jin, Y.; Wang, J.; Friend, R. H.; Gao, F., Metal halide perovskites for light-emitting diodes, *Nat. Mater.* **2020**.
36. Spanopoulos, I.; Hadar, I.; Ke, W.; Guo, P.; Sidhik, S.; Kepenekian, M.; Even, J.; Mohite, A. D.; Schaller, R. D.; Kanatzidis, M. G., Water-Stable 1D Hybrid Tin(II) Iodide Emits Broad Light with 36% Photoluminescence Quantum Efficiency, *J. Am. Chem. Soc.* **2020,** *142*, 9028-9038.
37. Wang, A.; Guo, Y.; Zhou, Z.; Niu, X.; Wang, Y.; Muhammad, F.; Li, H.; Zhang, T.; Wang, J.; Nie, S.; Deng, Z., Aqueous acid-based synthesis of lead-free tin halide perovskites with near-unity photoluminescence quantum efficiency, *Chem. Sci.* **2019,** *10*, 4573-4579.
38. Zhou, C.; Tian, Y.; Yuan, Z.; Lin, H.; Chen, B.; Clark, R.; Dilbeck, T.; Zhou, Y.; Hurley, J.; Neu, J.; Besara, T.; Siegrist, T.; Djurovich, P.; Ma, B., Highly Efficient Broadband Yellow Phosphor Based on Zero-Dimensional Tin Mixed-Halide Perovskite, *ACS Appl. Mater. Interfaces* **2017,** *9*, 44579-44583.
39. Lai, M. L.; Tay, T. Y. S.; Sadhanala, A.; Dutton, S. E.; Li, G.; Friend, R. H.; Tan, Z.-K., Tunable Near-Infrared Luminescence in Tin Halide Perovskite Devices, *J. Phys. Chem. Lett.* **2016,** *7*, 2653-2658.
40. Xing, G.; Kumar, M. H.; Chong, W. K.; Liu, X.; Cai, Y.; Ding, H.; Asta, M.; Grätzel, M.; Mhaisalkar, S.; Mathews, N.; Sum, T. C., Solution-Processed Tin-Based Perovskite for Near-Infrared Lasing, *Adv. Mater.* **2016,** *28*, 8191-8196.
41. Xiao, Z.; Kerner, R. A.; Zhao, L.; Tran, N. L.; Lee, K. M.; Koh, T.-W.; Scholes, G. D.; Rand, B. P., Efficient perovskite light-emitting diodes featuring nanometre-sized crystallites, *Nat. Photon.* **2017,** *11*, 108-115.
42. Lemmerer, A.; Billing, D. G., Lead halide inorganic-organic hybrids incorporating diammonium cations, *CrystEngComm* **2012,** *14*, 1954-1966.
43. Spanopoulos, I.; Hadar, I.; Ke, W.; Tu, Q.; Chen, M.; Tsai, H.; He, Y.; Shekhawat, G.; Dravid, V. P.; Wasielewski, M. R.; Mohite, A. D.; Stoumpos, C. C.; Kanatzidis, M. G., Uniaxial Expansion of the 2D Ruddlesden–Popper Perovskite Family for Improved Environmental Stability, *J. Am. Chem. Soc.* **2019,** *141*, 5518-5534.
44. Schueller, E. C.; Laurita, G.; Fabini, D. H.; Stoumpos, C. C.; Kanatzidis, M. G.; Seshadri, R., Crystal Structure Evolution and Notable Thermal Expansion in Hybrid Perovskites Formamidinium Tin Iodide and Formamidinium Lead Bromide, *Inorg. Chem.* **2018,** *57*, 695-701.
45. Whitfield, P. S.; Herron, N.; Guise, W. E.; Page, K.; Cheng, Y. Q.; Milas, I.; Crawford, M. K., Structures, Phase Transitions and Tricritical Behavior of the Hybrid Perovskite Methyl Ammonium Lead Iodide, *Sci. Rep.* **2016,** *6*, 35685.
46. Ong, K. P.; Goh, T. W.; Xu, Q.; Huan, A., Structural Evolution in Methylammonium Lead Iodide $CH_3NH_3PbI_3$, *J. Phys. Chem. A* **2015,** *119*, 11033-11038.
47. Fabini, D. H.; Stoumpos, C. C.; Laurita, G.; Kaltzoglou, A.; Kontos, A. G.; Falaras, P.; Kanatzidis, M. G.; Seshadri, R., Reentrant Structural and Optical Properties and Large Positive Thermal Expansion in Perovskite Formamidinium Lead Iodide, *Angew. Chem., Int. Ed.* **2016,** *55*, 15392-15396.
48. Weber, O. J.; Ghosh, D.; Gaines, S.; Henry, P. F.; Walker, A. B.; Islam, M. S.; Weller, M. T., Phase

Behavior and Polymorphism of Formamidinium Lead Iodide, *Chem. Mater.* **2018,** *30*, 3768-3778.
49. Simenas, M.; Balciunas, S.; Wilson, J. N.; Svirskas, S.; Kinka, M.; Garbaras, A.; Kalendra, V.; Gagor, A.; Szewczyk, D.; Sieradzki, A.; Maczka, M.; Samulionis, V.; Walsh, A.; Grigalaitis, R.; Banys, J., Suppression of phase transitions and glass phase signatures in mixed cation halide perovskites, *Nat. Commun.* **2020,** *11*, 5103.
50. Fung, K. Z.; Virkar, A. V., Phase Stability, Phase Transformation Kinetics, and Conductivity of Y_2O_3—Bi_2O_3 Solid Electrolytes Containing Aliovalent Dopants, *J. Am. Ceram. Soc.* **1991,** *74*, 1970-1980.
51. Ding, H.; Virkar, A. V.; Liu, F., Defect configuration and phase stability of cubic versus tetragonal yttria-stabilized zirconia, *Solid State Ionics* **2012,** *215*, 16-23.
52. Jiang, B.; Grande, T.; Selbach, S. M., Local Structure of Disordered Bi0.5K0.5TiO3 Investigated by Pair Distribution Function Analysis and First-Principles Calculations, *Chem. Mater.* **2017,** *29*, 4244-4252.
53. Young, C. A.; Goodwin, A. L., Applications of pair distribution function methods to contemporary problems in materials chemistry, *J. Mater. Chem.* **2011,** *21*, 6464-6476.
54. Billinge, S. J. L.; Kanatzidis, M. G., Beyond crystallography: the study of disorder, nanocrystallinity and crystallographically challenged materials with pair distribution functions, *Chem. Commun.* **2004**, 749-760.
55. Stoumpos, C. C.; Cao, D. H.; Clark, D. J.; Young, J.; Rondinelli, J. M.; Jang, J. I.; Hupp, J. T.; Kanatzidis, M. G., Ruddlesden–Popper Hybrid Lead Iodide Perovskite 2D Homologous Semiconductors, *Chem. Mater.* **2016,** *28*, 2852-2867.
56. Battle, P. D.; Green, M. A.; Lago, J.; Millburn, J. E.; Rosseinsky, M. J.; Vente, J. F., Crystal and Magnetic Structures of $Ca_4Mn_3O_{10}$, an n = 3 Ruddlesden−Popper Compound, *Chem. Mater.* **1998,** *10*, 658-664.
57. Mao, L.; Ke, W.; Pedesseau, L.; Wu, Y.; Katan, C.; Even, J.; Wasielewski, M. R.; Stoumpos, C. C.; Kanatzidis, M. G., Hybrid Dion–Jacobson 2D Lead Iodide Perovskites, *J. Am. Chem. Soc.* **2018,** *140*, 3775-3783.
58. Dion, M.; Ganne, M.; Tournoux, M., Nouvelles familles de phases $M^{I}M^{II}{}_2Nb_3O_{10}$ a feuillets "perovskites", *Mater. Res. Bull.* **1981,** *16*, 1429-1435.
59. Soe, C. M. M.; Stoumpos, C. C.; Kepenekian, M.; Traoré, B.; Tsai, H.; Nie, W.; Wang, B.; Katan, C.; Seshadri, R.; Mohite, A. D.; Even, J.; Marks, T. J.; Kanatzidis, M. G., New Type of 2D Perovskites with Alternating Cations in the Interlayer Space, $(C(NH_2)_3)(CH_3NH_3)_nPb_nI_{3n+1}$: Structure, Properties, and Photovoltaic Performance, *J. Am. Chem. Soc.* **2017,** *139*, 16297-16309.
60. Li, S.; Zhu, Q.; Li, X.; Sun, X.; Li, J.-G., Near-infrared emitting microspheres of $LaAlO_3$:Mn^{4+}: Defects engineering via Ge^{4+} doping for greatly enhanced luminescence and improved afterglow, *J. Alloys Compd.* **2020,** *827*, 154365.
61. Cortecchia, D.; Mróz, W.; Neutzner, S.; Borzda, T.; Folpini, G.; Brescia, R.; Petrozza, A., Defect Engineering in 2D Perovskite by Mn(II) Doping for Light-Emitting Applications, *Chem* **2019,** *5*, 2146-2158.
62. Seth, S.; Ahmed, T.; De, A.; Samanta, A., Tackling the Defects, Stability, and Photoluminescence of $CsPbX_3$ Perovskite Nanocrystals, *ACS Energy Lett.* **2019,** *4*, 1610-1618.
63. Luo, J.; Wang, X.; Li, S.; Liu, J.; Guo, Y.; Niu, G.; Yao, L.; Fu, Y.; Gao, L.; Dong, Q.; Zhao, C.; Leng, M.; Ma, F.; Liang, W.; Wang, L.; Jin, S.; Han, J.; Zhang, L.; Etheridge, J.; Wang, J.; Yan, Y.; Sargent, E. H.; Tang, J., Efficient and stable emission of warm-white light from lead-free halide double perovskites, *Nature* **2018,** *563*, 541-545.
64. Sun, C.; Gao, Z.; Deng, Y.; Liu, H.; Wang, L.; Su, S.; Li, P.; Li, H.; Zhang, Z.; Bi, W., Orange to Red, Emission-Tunable Mn-Doped Two-Dimensional Perovskites with High Luminescence and Stability, *ACS Appl. Mater. Interfaces* **2019,** *11*, 34109-34116.
65. Pimputkar, S.; Speck, J. S.; DenBaars, S. P.; Nakamura, S., Prospects for LED lighting, *Nat. Photon.* **2009,** *3*, 180.
66. Ferreira, A. C.; Létoublon, A.; Paofai, S.; Raymond, S.; Ecolivet, C.; Rufflé, B.; Cordier, S.; Katan, C.; Saidaminov, M. I.; Zhumekenov, A. A.; Bakr, O. M.; Even, J.; Bourges, P., Elastic Softness of Hybrid Lead Halide Perovskites, *Phys. Rev. Lett.* **2018,** *121*, 085502.
67. Wright, A. D.; Verdi, C.; Milot, R. L.; Eperon, G. E.; Pérez-Osorio, M. A.; Snaith, H. J.; Giustino, F.; Johnston, M. B.; Herz, L. M., Electron–phonon coupling in hybrid lead halide perovskites, *Nat. Commun.* **2016,** *7*, 11755.
68. Neukirch, A. J.; Abate, I. I.; Zhou, L.; Nie, W.; Tsai, H.; Pedesseau, L.; Even, J.; Crochet, J. J.; Mohite, A. D.; Katan, C.; Tretiak, S., Geometry Distortion and Small Polaron Binding Energy Changes with Ionic Substitution in Halide Perovskites, *J. Phys. Chem. Lett.* **2018,** *9*, 7130-7136.

69. Harwell, J. R.; Baikie, T. K.; Baikie, I. D.; Payne, J. L.; Ni, C.; Irvine, J. T. S.; Turnbull, G. A.; Samuel, I. D. W., Probing the energy levels of perovskite solar cells via Kelvin probe and UV ambient pressure photoemission spectroscopy, *Phys. Chem. Chem. Phys.* **2016,** *18*, 19738-19745.
70. Mao, L.; Guo, P.; Kepenekian, M.; Hadar, I.; Katan, C.; Even, J.; Schaller, R. D.; Stoumpos, C. C.; Kanatzidis, M. G., Structural Diversity in White-Light-Emitting Hybrid Lead Bromide Perovskites, *J. Am. Chem. Soc.* **2018,** *140*, 13078-13088.
71. Smith, M. D.; Jaffe, A.; Dohner, E. R.; Lindenberg, A. M.; Karunadasa, H. I., Structural origins of broadband emission from layered Pb–Br hybrid perovskites, *Chem. Sci.* **2017,** *8*, 4497-4504.
72. Li, X.; Guo, P.; Kepenekian, M.; Hadar, I.; Katan, C.; Even, J.; Stoumpos, C. C.; Schaller, R. D.; Kanatzidis, M. G., Small Cyclic Diammonium Cation Templated (110)-Oriented 2D Halide (X = I, Br, Cl) Perovskites with White-Light Emission, *Chem. Mater.* **2019,** *31*, 3582-3590.
73. Gautier, R.; Paris, M.; Massuyeau, F., Exciton Self-Trapping in Hybrid Lead Halides: Role of Halogen, *J. Am. Chem. Soc.* **2019,** *141*, 12619-12623.
74. Li, X.; Wu, Y.; Zhang, S.; Cai, B.; Gu, Y.; Song, J.; Zeng, H., $CsPbX_3$ Quantum Dots for Lighting and Displays: Room-Temperature Synthesis, Photoluminescence Superiorities, Underlying Origins and White Light-Emitting Diodes, *Adv. Funct. Mater.* **2016,** *26*, 2435-2445.
75. Yuan, Z.; Zhou, C.; Tian, Y.; Shu, Y.; Messier, J.; Wang, J. C.; van de Burgt, L. J.; Kountouriotis, K.; Xin, Y.; Holt, E.; Schanze, K.; Clark, R.; Siegrist, T.; Ma, B., One-dimensional organic lead halide perovskites with efficient bluish white-light emission, *Nat. Commun.* **2017,** *8*, 14051.
76. Thirumal, K.; Chong, W. K.; Xie, W.; Ganguly, R.; Muduli, S. K.; Sherburne, M.; Asta, M.; Mhaisalkar, S.; Sum, T. C.; Soo, H. S.; Mathews, N., Morphology-Independent Stable White-Light Emission from Self-Assembled Two-Dimensional Perovskites Driven by Strong Exciton–Phonon Coupling to the Organic Framework, *Chem. Mater.* **2017,** *29*, 3947-3953.
77. Zhou, G.; Li, M.; Zhao, J.; Molokeev, M. S.; Xia, Z., Single-Component White-Light Emission in 2D Hybrid Perovskites with Hybridized Halogen Atoms, *Adv. Optical Mater.* **2019,** *7*, 1901335.
78. Lian, L.; Zheng, M.; Zhang, P.; Zheng, Z.; Du, K.; Lei, W.; Gao, J.; Niu, G.; Zhang, D.; Zhai, T.; Jin, S.; Tang, J.; Zhang, X.; Zhang, J., Photophysics in $Cs_3Cu_2X_5$ (X = Cl, Br, or I): Highly Luminescent Self-Trapped Excitons from Local Structure Symmetrization, *Chem. Mater.* **2020,** *32*, 3462-3468.
79. Febriansyah, B.; Giovanni, D.; Ramesh, S.; Koh, T. M.; Li, Y.; Sum, T. C.; Mathews, N.; England, J., Inducing formation of a corrugated, white-light emitting 2D lead-bromide perovskite via subtle changes in templating cation, *J. Mater. Chem. C* **2020,** *8*, 889-893.
80. Paternò, G. M.; Mishra, N.; Barker, A. J.; Dang, Z.; Lanzani, G.; Manna, L.; Petrozza, A., Broadband Defects Emission and Enhanced Ligand Raman Scattering in 0D Cs3Bi2I9 Colloidal Nanocrystals, *Adv. Funct. Mater.* **2019,** *29*, 1805299.
81. Shakfa, M. K.; Wiemer, M.; Ludewig, P.; Jandieri, K.; Volz, K.; Stolz, W.; Baranovskii, S. D.; Koch, M., Thermal quenching of photoluminescence in Ga(AsBi), *J. Appl. Phys.* **2015,** *117*, 025709.
82. Rubel, O.; Baranovskii, S. D.; Hantke, K.; Kunert, B.; Rühle, W. W.; Thomas, P.; Volz, K.; Stolz, W., Model of temperature quenching of photoluminescence in disordered semiconductors and comparison to experiment, *Phys. Rev. B* **2006,** *73*, 233201.

Figures

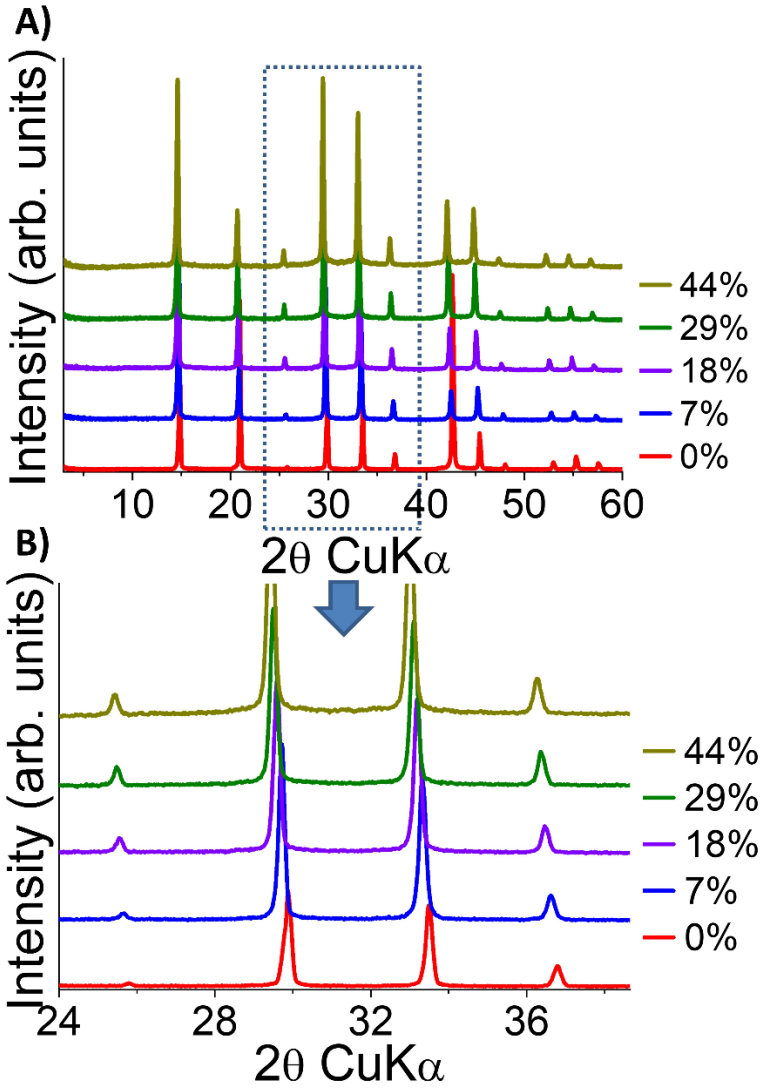

Figure 1. A) Comparison of experimental PXRD patterns of the $(FA)_{1-x}(en)_x(Pb)_{1-0.7x}(Br)_{3-0.4x}$ compounds with increasing amount of *en* (x = 0%, 7%, 18%, 29%, 44%). All materials regardless of x-value are isostructural to cubic α-$FAPbBr_3$ perovskite. B) zoom into the highlighted area of the PXRD patterns from 24° to 37° 2θ showing the shift of the diffraction peaks to lower degrees 2θ with increasing *en* loading, signaling a unit cell expansion.

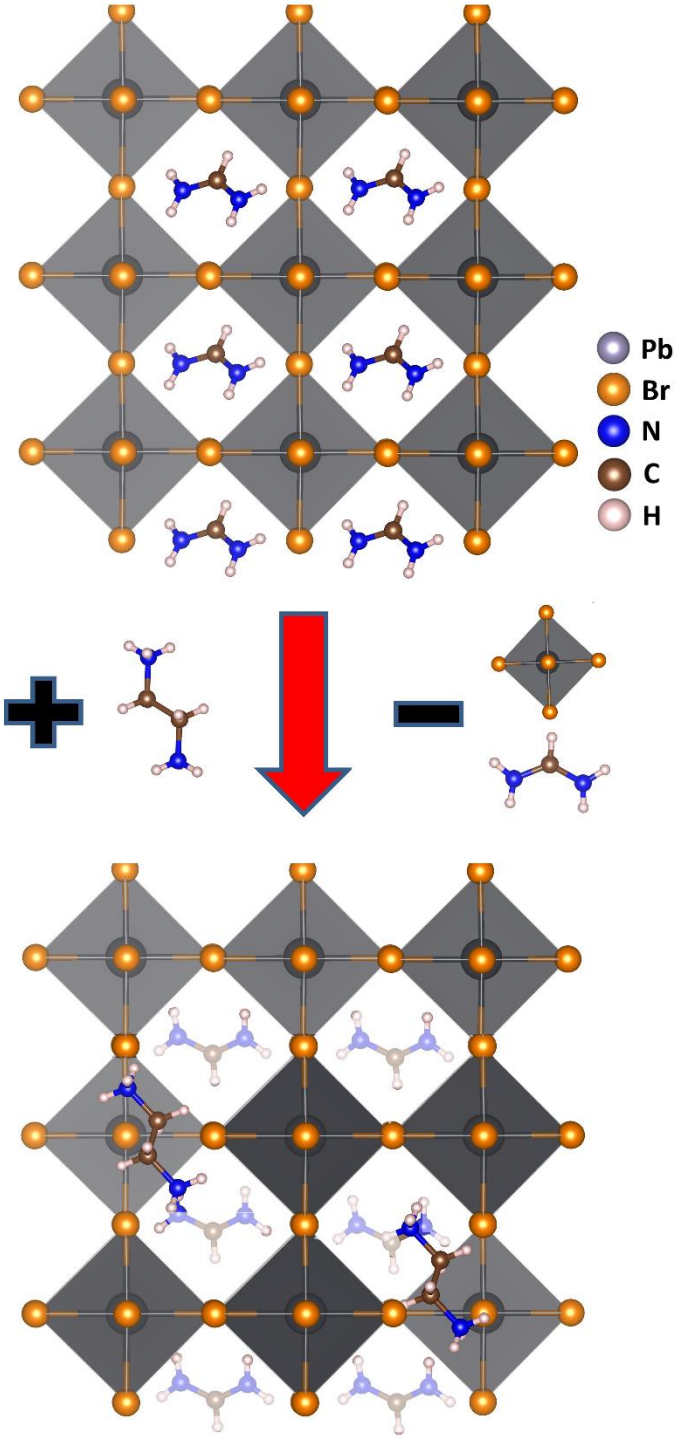

Figure 2. Potential structural representation of the single crystal structure of the hollow materials. In order for ethylenediammonium cations to be incorporated in the lattice without structural deformation, $[PbBr_6]^{4-}$ octahedra and formamidinium cations must be expelled from the structure.

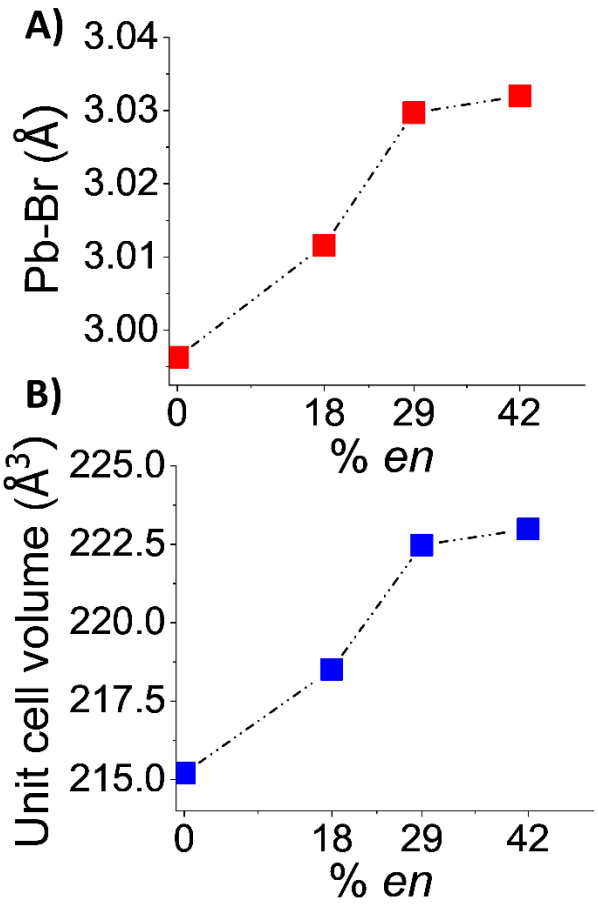

Figure 3. Correlation between the A) Pb-Br bond lengths and B) unit cell volume to the amount of incorporated *en* based on single crystal XRD studies.

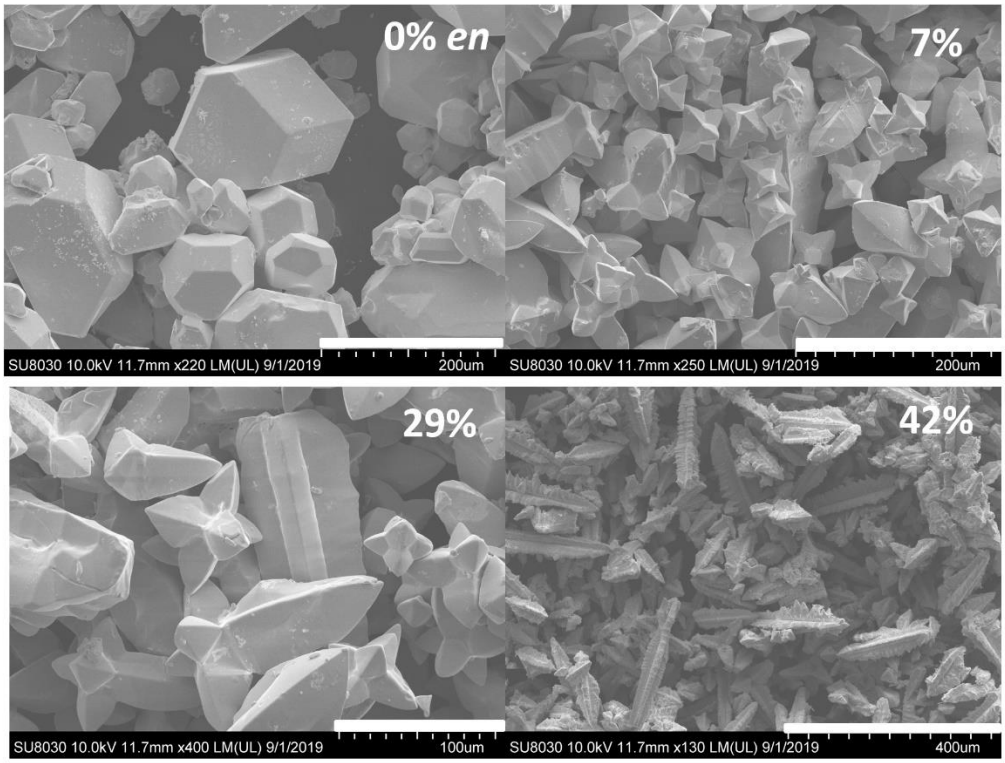

Figure 4. Representative SEM images of as made $(FA)_{1-x}(en)_x(Pb)_{1-0.7x}(Br)_{3-0.4x}$ perovskites for x = 0%, 7%, 29%, 42%, respectively. At high *en* loading spear like crystals based on intergrowths of crystal octahedra are observed.

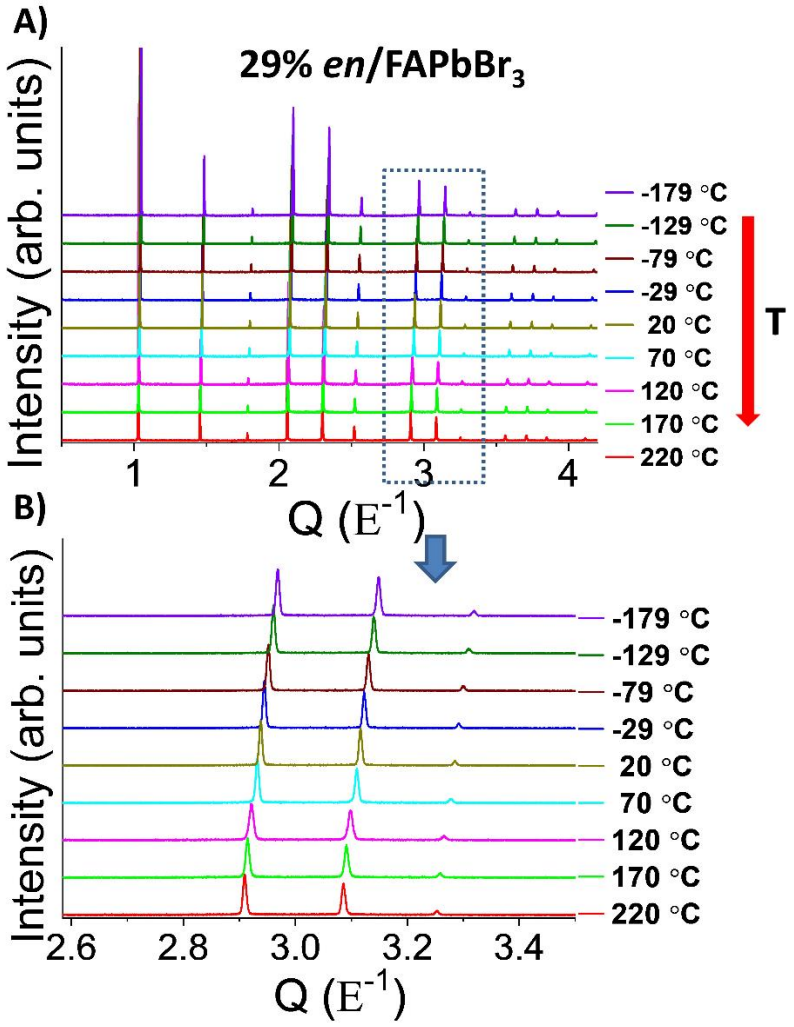

Figure 5. A) High resolution variable temperature PXRD patterns for the 29% *en*/$FAPbBr_3$, consisting of one heating cycle. B) The highlighted area is enlarged to show better the shift of the diffraction peaks to lower Q values with increasing temperature, indicative of lattice thermal expansion. There is no appearance of additional diffraction peaks, revealing the absence of temperature dependent structural phase transitions.

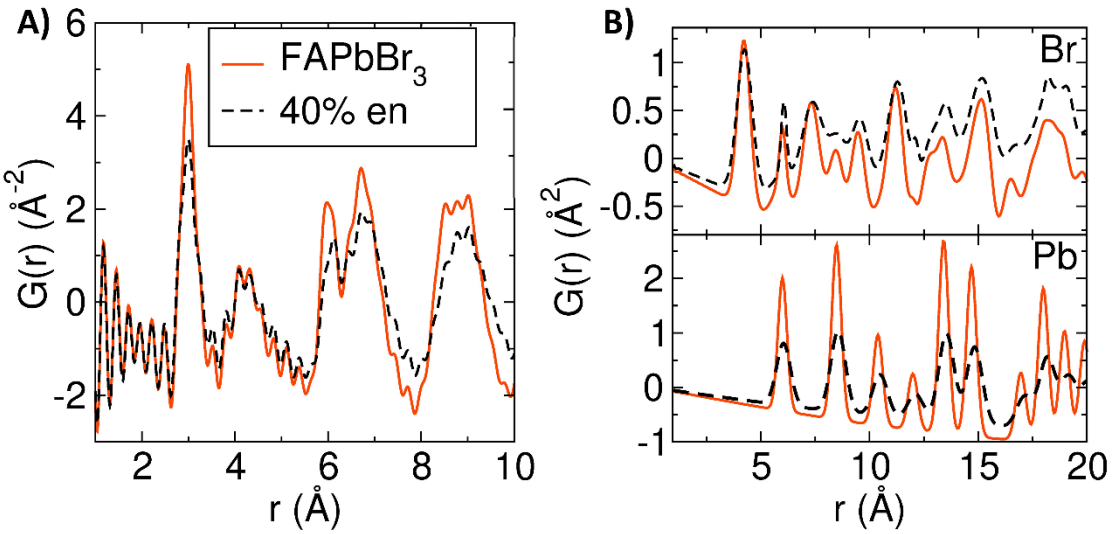

Figure 6. A) PDF comparison of the pristine $FAPbBr_3$, solid orange line, and 40% *en*/ $FAPbBr_3$, black dashed lines. B) Partial PDF fits of pristine $FAPbBr_3$ and 40% *en*/ $FAPbBr_3$ describing (top) Br-Br correlations and (bottom) Pb-Pb correlations.

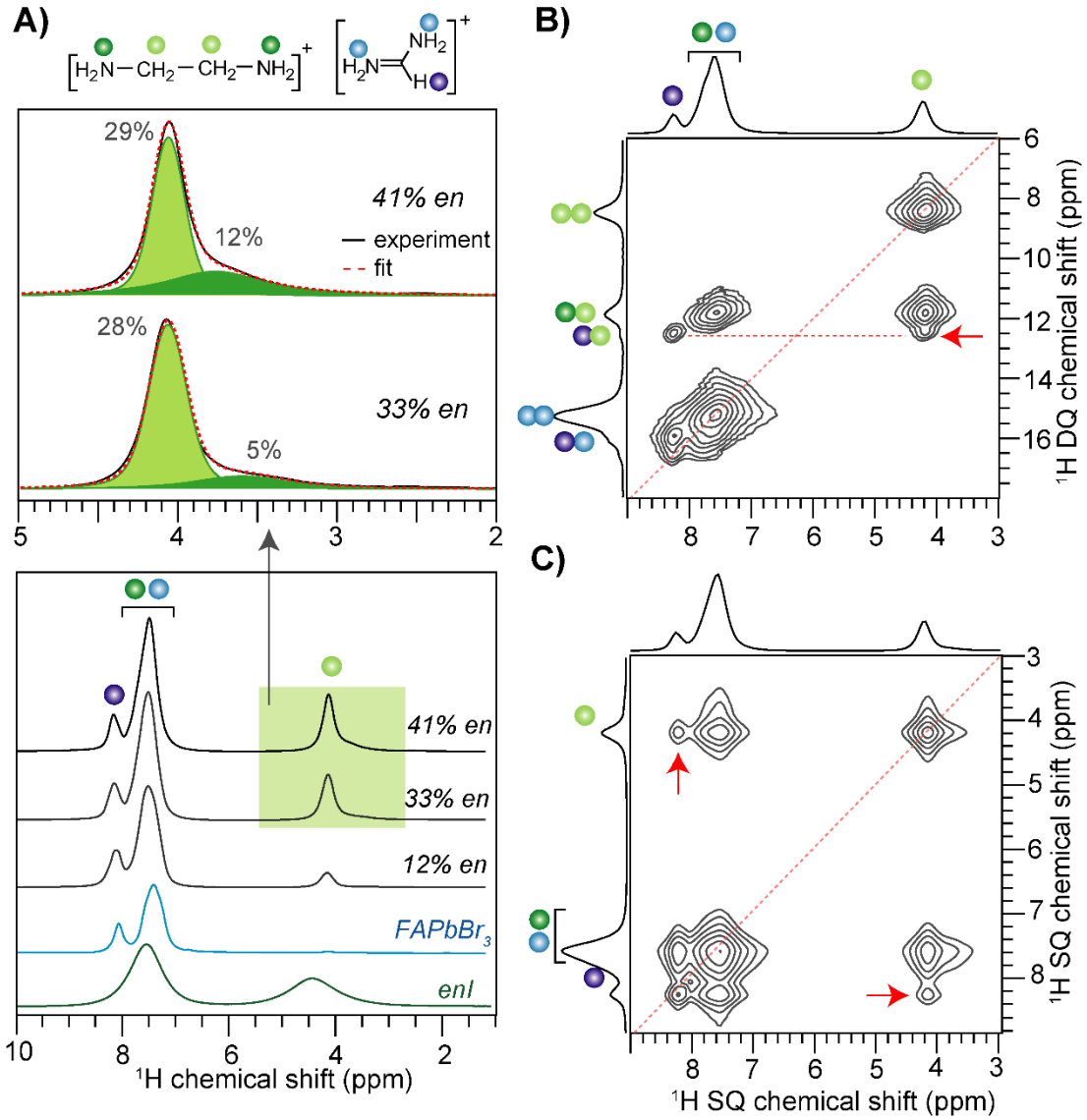

Figure 7. Solid-state ^{1}H MAS NMR spectra of $FAPbBr_3$ and hollow perovskites acquired of at 18.8 T (Larmor frequency of ^{1}H is 850.1 MHz) and at RT with 35 kHz MAS. A) Comparison of 1D ^{1}H MAS NMR spectra of $FAPbBr_3$, 12% *en*/$FAPbBr_3$, 33% *en*/$FAPbBr_3$ and 41% *en*/$FAPbBr_3$. Signals correspond to FA^{+} and en^{+} protons are depicted in color dots as shown in the Figure inset. B) 2D ^{1}H-^{1}H DQ-SQ correlation NMR spectra of 41% *en*/$FAPbBr_3$ using DQ excitation time of 28.6 µs. C) 2D ^{1}H-^{1}H SQ-SQ correlation NMR spectra of 41% *en*/$FAPbBr_3$ using spin diffusion mixing time of 100 ms.

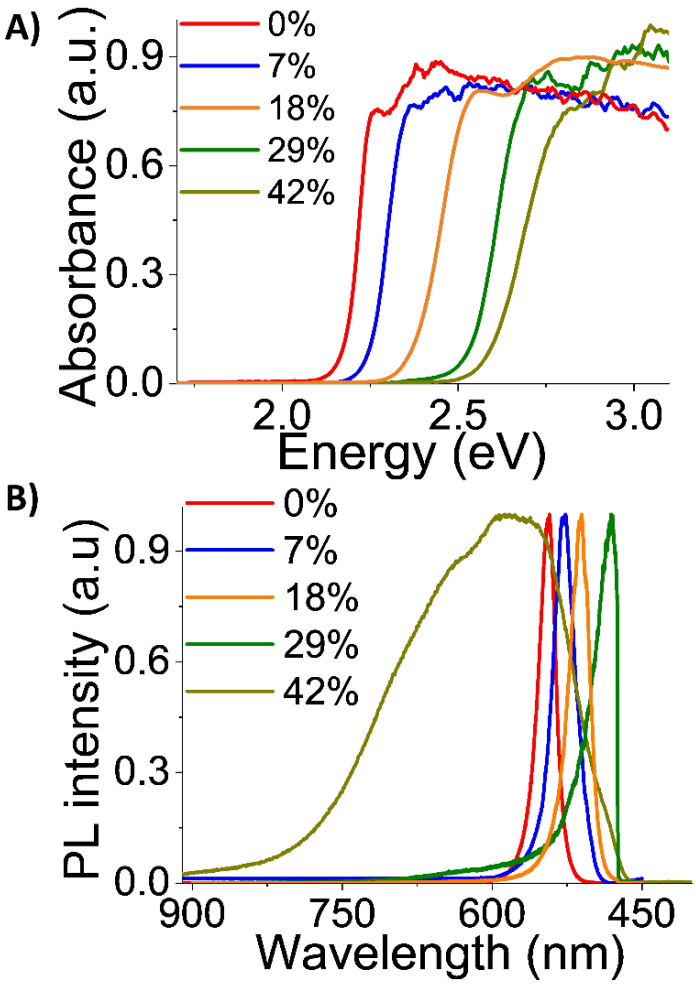

Figure 8. A) Optical absorption and B) emission spectra of compounds $(FA)_{1-x}(en)_x(Pb)_{1-0.7x}(Br)_{3-0.4x}$, with increasing amount of *en*.

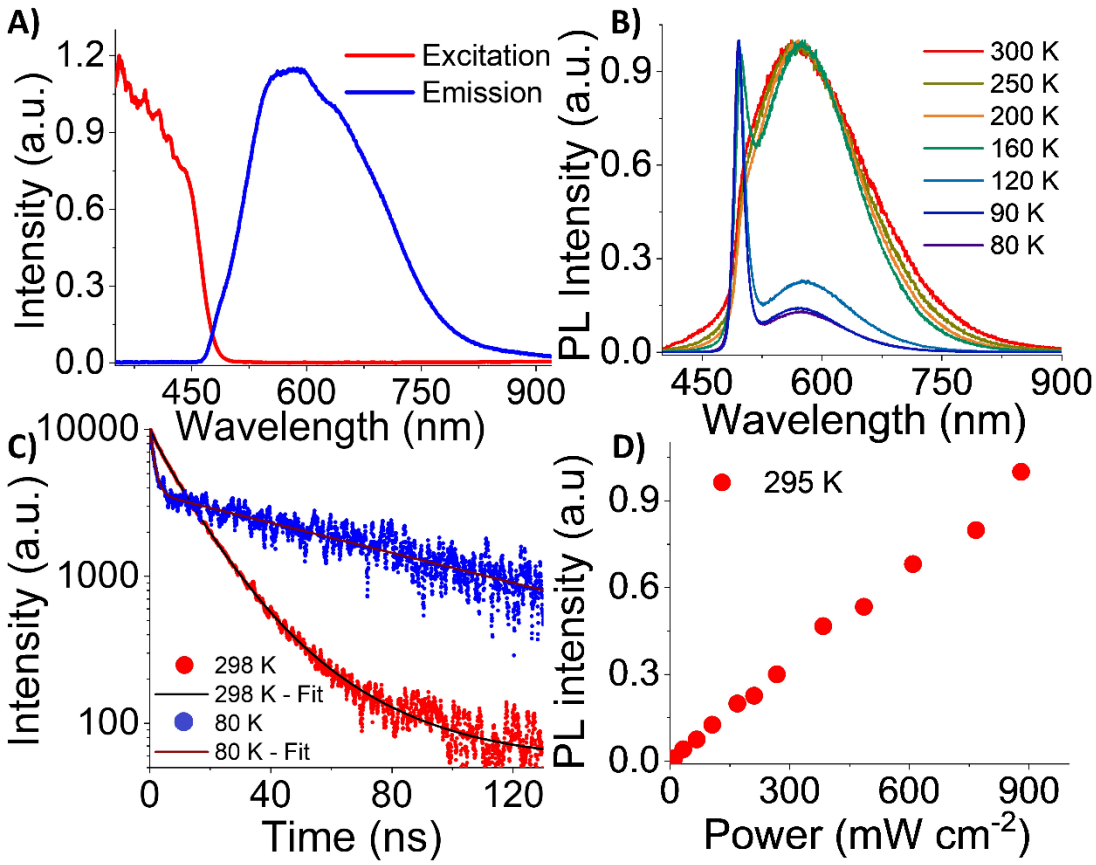

Figure 9. A) The recorded absorption and emission spectra of 42% *en*/$FAPbBr_3$ compound at RT, B) temperature dependent PL measurements from 300K to 80K (normalized), C) Time-resolved photoluminescence decay at 80K and 298K, D) Emission intensity versus excitation power, revealing the linear correlation of PL intensity with increasing power. The differences of the PL emission spectra at RT in A) and B) are ascribed to the different instrumentation set up and excitation wavelength used.

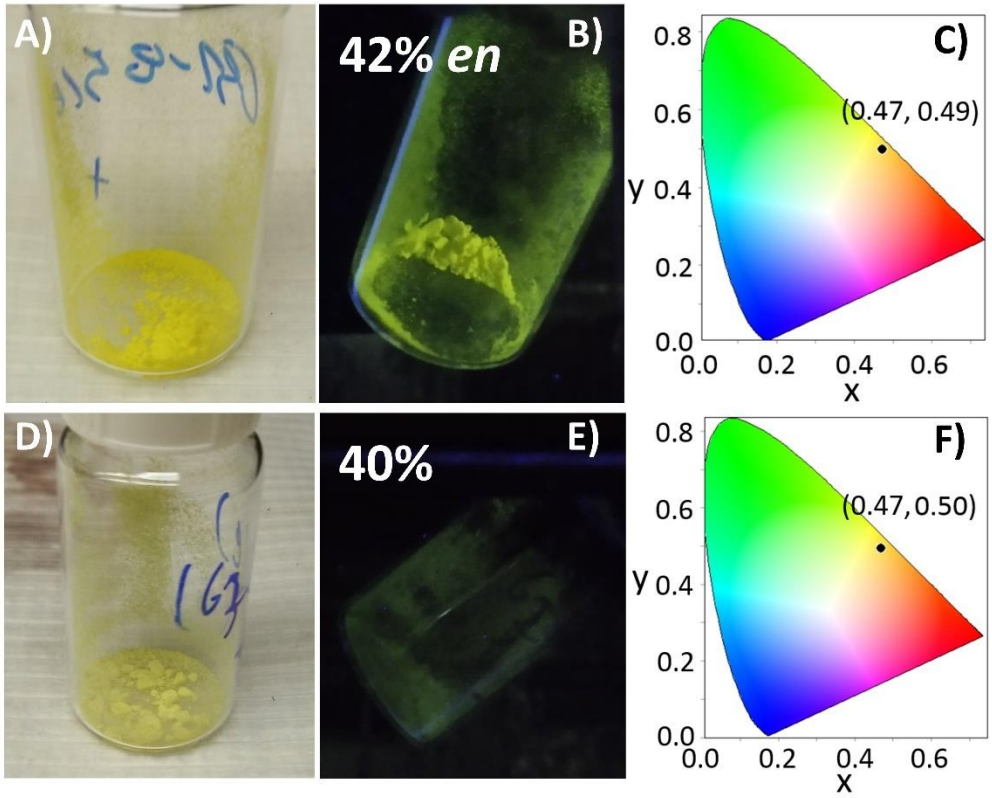

Figure 10. Photographs of dried single crystals of 42% *en*/$FAPbBr_3$ and 40% *en*/$FAPbBr_3$ samples, under ambient light A), D), and under UV light B), E) respectively. CIE chromaticity coordinates C) and F) for the corresponding compounds respectively.

Table 1. Crystal and Structure Refinement Data for $(FA)_{1-x}(en)_x(Pb)_{1-0.7x}(Br)_{3-0.4x}$ (x= 0%, 18%, 29%, 42%) at 293K.

Sample name	**α-FAPbBr$_3$**	**18% *en***	**29% *en***	**42% *en***
Temperature	293K	293K	293K	293K
Crystal system	cubic	cubic	cubic	cubic
Space group	*Pm*-3*m*	*Pm*-3*m*	*Pm*-3*m*	*Pm*-3*m*
Unit cell dimensions	a = 5.9926(3) Å, α = 90° b = 5.9926(3) Å, β = 90° c = 5.9926(3) Å, γ = 90°	a = 6.02320(10) Å, α = 90° b = 6.02320(10) Å, β = 90° c = 6.02320(10) Å, γ = 90°	a = 6.0594(2) Å, α = 90° b = 6.0594(2) Å, β = 90° c = 6.0594(2) Å, γ = 90°	a = 6.06400(10) Å, α = 90° b = 6.06400(10) Å, β = 90° c = 6.06400(10) Å, γ = 90°
Volume	215.202(19) Å^3	218.515(6) Å^3	222.479(13) Å^3	222.986(6) Å^3
Z	1	1	1	1
Density (calculated)	3.7574 g/cm^3	3.5729 g/cm^3	3.3631 g/cm^3	3.3177 g/cm^3
Independent reflections	86 [R_{int} = 0.0395]	95 [R_{int} = 0.0224]	105 [R_{int} = 0.0228]	90 [R_{int} = 0.0208]
Completeness to θ = 29.33°	98%	98%	97%	100%
Data / restraints / parameters	86 / 1 / 8	95 / 1 / 7	105 / 1 / 7	90 / 1 / 7
Goodness-of-fit	1.53	1.95	2.96	2.67
Final R indices [I>2σ(I)]	R_{obs} = 0.0223, wR_{obs} = 0.0513	R_{obs} = 0.0189, wR_{obs} = 0.0518	R_{obs} = 0.0251, wR_{obs} = 0.0715	R_{obs} = 0.0267, wR_{obs} = 0.0692
R indices [all data]	R_{all} = 0.0235, wR_{all} = 0.0516	R_{all} = 0.0189, wR_{all} = 0.0518	R_{all} = 0.0252, wR_{all} = 0.0715	R_{all} = 0.0267, wR_{all} = 0.0692
Largest diff. peak and hole	0.67 and -0.82 e·Å^{-3}	0.61 and -0.47 e·Å^{-3}	0.79 and -0.40 e·Å^{-3}	0.87 and -0.29 e·Å^{-3}

$R = \Sigma||F_o|-|F_c|| / \Sigma|F_o|$, $wR = (\Sigma[w(|F_o|^2 - |F_c|^2)^2] / \Sigma[w(|F_o|^4)])^{1/2}$ and $w=1/(\sigma^2(I)+0.0004I^2)$

Table 2. Comparison of the refined unit cell dimensions of $(FA)_{1-x}(en)_x(Pb)_{1-0.7x}(Br)_{3-0.4x}$ materials along with their determined band gaps. The increase of the *en* concentration leads to an increase to the unit cell dimensions and a blue shift of the band gap for all materials. The unit cell dimensions of the 7% *en* sample were determined from indexing of the PXRD patterns.

$FAPbBr_3$ + *en*%	**Unit cell parameters a (Å)**	**Unit cell Volume ($Å^3$)**	**Band gap (eV)**
0	5.9926(3)	215.202(19)	2.20
7	6.0046(2)	216.00(2)	2.25
18	6.02320(10)	218.515(6)	2.36
29	6.0594(2)	222.479(13)	2.54
42	6.06400(10)	222.986(6)	2.60

Table 3. Photophysical properties of the bulk crystals of the 42% *en*/$FAPbBr_3$ compound. (τ_{av} is the average PL lifetime).

42% *en*/$FAPbBr_3$	**T(K)**	**PLQY (%)**	**τ_{av} (ns)**	**FWHM (nm)**	**CRI**	**CCT (K)**	**CIE**
Crystals	298K	1	15	195	67	3144	(0.47,0.49)

Table of Contents Graphic